(Received 12 March 2026, Accepted 11 June 2026, Scheduled 30 June 2026)

Comprehensive Design Method of High-Performance Energy-Selective Structure Based on Stacked Slotline

Huan Jiang[1], Yanlin Xu[1,*], Tao Tian[1], Bowen Deng[2], Hao Ding[1], and Peiguo Liu[1]

[1] *The College of Electronic Science and Technology, National University of Defense Technology, China*
[2] *China Aerodynamics Research and Development Center (CARDC), China*

ABSTRACT: This paper presents a high-performance energy-selective structure (ESS) design methodology based on a stacked slotline. By leveraging the unique characteristics of three-dimensional stacked structures, the method efficiently converts spatial waves into guided waves in slotline transmission lines, which can be tailored via lumped-circuit design to achieve precise energy-selective functionality. The proposed design approach systematically extends previous work by providing a clear theoretical foundation for decoupling and independently optimizing multiple ESS performance indicators. This allows the design of structures with flexibly selectable frequency bands and high shielding efficiency. Two prototypes were fabricated to validate the method. Prototype I targets bandwidth expansion, achieving an operational range from 2.2 to 8.2 GHz (115.4% relative bandwidth), with less than 1 dB insertion loss and over 10 dB shielding effectiveness across the band. Prototype II emphasizes shielding performance, reaching a shielding efficiency greater than 33 dB between 3.9 and 6.3 GHz, with a maximum of 40.3 dB. Both prototypes were fabricated and validated through experimental measurements, showing agreement with the simulation results. The performance of the two designed structures far exceeds other existing ESSs in terms of broadband or high shielding efficiency, indicating that the comprehensive design method has great potential to significantly improve the design of targeted technical specifications.

1. INTRODUCTION

Microwave systems are progressively advancing towards higher efficiency and enhanced sensitivity. However, electronic systems and devices have become increasingly susceptible to disturbances in harsh electromagnetic (EM) environments. Notably, signals with high energy densities may cause destructive current and voltage surges within the device, leading to irreversible damage [1, 2].

Conventionally, EM shielding methods primarily encompass energy-domain circuit protection devices, such as limiters [3, 4]. Frequency-domain protection methods are represented by filters [5, 6] and frequency-selective surfaces (FSSs) [7–9]. However, from an energy perspective, conventional methods fail to discriminate between potentially damaging high-energy-density signals and weaker yet critical signals required for wireless communication.

To efficiently offer adaptive protection against unexpected intense electromagnetic (EM) threats across various energy levels, the concept of an energy-selective structure (ESS) was introduced in 2009 by Liu's team [10–13]. The energy-selective protection method represents a novel approach to high-power microwave protection. It employs impedance-variable materials or devices that adaptively adjust their impedance in response to the intensity of the spatial EM waves. This adaptive behavior allows for switching the working state, enabling the normal reception of operational signals while effectively blocking high-energy-density signals. Consequently, a shielding effect was achieved within the specified bandwidth.

Energy-selective surface is a type of metasurface. The traditional metasurface design is based on two-dimensional (2D) monolayer structure design, which is easy to design and process. However, 2D metasurfaces have significant limitations that cannot be ignored. Among them, the filtering characteristics within the passband of monolayer FSS are poor; the passband bandwidth of single-layer energy-selective protective structure is narrow; the shielding effectiveness of the protective state is limited; and the absorption rate of single-layer absorbing metasurfaces is limited. In short, a small degree of freedom in single-layer structure design can lead to unsatisfactory performance design and difficulty in expanding functionality.

Another 2D structure composed of multiple layers of nonresonant surfaces can achieve high-order filtering response with very low contours [14–16]. Although a generalized synthesis method based on classical empirical formulas has been proposed for such multi-layer 2D structures, which has improved the accuracy of the synthesis process. However, due to the strong coupling between different layers that cannot be ignored, only an approximate relationship between the circuit and physical parameters has been established, and further extensive optimization should be carried out.

Three-dimensional (3D) structures offer an expanded range of freedoms, enabling the creation of superior characteristics, including high-order filtering responses, broadband performance, optimized protection efficiency, increased absorption rate, etc. Inspired by the analysis methods developed for

* Corresponding author: Yanlin Xu (13298656824@163.com).

FSSs, substrate-integrated waveguide (SIW)-based cavity-type frequency-selective surfaces (FSSs) were introduced to realize multimode resonances [14]. Subsequent studies designed higher-order FSSs with quasi-elliptic bandpass responses using coupling matrix synthesis [17]. Later, a systematic synthesis approach for SIW-based FSSs was proposed by introducing cross-coupling between SIW resonant cavities [18]. Nevertheless, such cavity-based FSSs fabricated using printed circuit board (PCB) technology still suffer from the constraint of standardized substrate thickness and generally require sufficient isolation between adjacent unit cells.

To overcome these limitations, planar transmission lines supporting quasi-TEM/TEM modes have also been explored as periodic guided-wave units. Since 2010, several guided-wave FSS configurations have been reported, including stacked microstrip lines, parallel-plate waveguides, and parallel-strip lines [19–21]. Compared with conventional 2D FSSs, these structures offer greater design flexibility and better control of spatial-to-guided-wave mode conversion, showing strong potential for high-performance structure design.

In recent years, in terms of energy selection structure design, 3D-ESS has received widespread attention due to its outstanding performance in broadband characteristics and high shielding efficiency (SE) [13, 22, 23]. Ref. [13] utilized the adjustable dispersion curve of Spoof Surface Plasmon Polariton (SSPP) combined with adaptive response nonlinear devices to achieve the switching of the protection state in the ultrawideband range of 6.7 GHz to 10.8 GHz. A 3D absorption ESS based on the installation of PIN limiting diodes has been proposed to achieve both high-power EM protection and low reflection, with a shielding efficiency of up to 40 dB at 3 GHz [22]. Ref. [23] proposed a preliminary idea of a stacked ESS based on a slotline, which effectively achieves 30 dB protection capability within 25.5% of the entire bandwidth. However, the problems of extracting key decoupling parameters and broadband design have not been solved. The above structure has made breakthroughs in both broadband and high-SE performance indicators, but both have insufficient performance indicators and cannot be applied to most scenarios.

In this study, a comprehensive design method for high-performance ESSs based on a stacked slotline structure integrated with nonlinear devices is proposed. This is achieved by loading the energy-selective circuit structure onto the slotline transmission line (TL). Through equivalent circuit model analysis and key parameter decoupling analysis, theoretically, it has achieved the design of bandwidth protection with flexibly selected ranges and broadband ultra-high SE. According to this method, two high-performance ESS samples were designed: one capable of achieving protection at a relative bandwidth of 115.4%, and the other capable of achieving shielding effectiveness above 33 dB within 47.1% bandwidth. The experimental results were consistent with the simulated ones, which fully demonstrated the effectiveness of the comprehensive design method of the structure and its great application potential in the field of high-power microwave protection.

The remainder of this paper is organized as follows. Section 2 reviews the basic properties and working principles of ESS with double resonance points based on slotlines. Section 3 provides basic design guidelines for utilizing the model structure and proposes an ultra-wideband design prototype and a high-SE prototype to verify the applicability of the method. Section 4 provides experimental demonstrations of the proposed method. Finally, conclusions are presented in Section 5.

2. CHARACTERISTIC ANALYSIS OF ENERGY-SELECTIVE STRUCTURE WITH DOUBLE RESONANT POINTS

Figure 1 shows a schematic of the structure with double resonant points. This study employs F4B boards, characterized by a dielectric constant of 2.65 and a loss tangent of 0.0013, as substrates. Single-sided etching of slotlines was utilized to load the lumped circuit. In this configuration, the xoy plane serves as the periodic plane, with the EM waves incident along the z-axis and the electric field direction aligned parallel to the y-axis.

The boundary conditions of the unit structure were converted into a perfect electric conductor (PEC) and a perfect magnetic conductor (PMC), and each unit was inserted into a parallel-plate waveguide. At this point, the characteristic impedance of the input and output ports is equal to that of the parallel-plate waveguide. As shown in Fig. 1(d), Z_0 can be represented by η as $\frac{\eta w}{2t_{\text{air}}+t}$, where Z_0 denotes the port impedance, η the free-space wave impedance, w the longitudinal height of the unit cell, t_{air} the thickness of the air layer, and t the substrate thickness. Furthermore, by relocating the input and output ports to both termini of the slotline and utilizing the characteristic pattern solver in Computer Simulation Technology Microwave Studio (CST-MWS), the characteristic impedance Z_s and equivalent electrical length l_s of the slotline structure can be extracted [24].

Note that the slotline structure can sense the strength of the energy entering the slotline by introducing nonlinear devices and perform adaptive impedance transformation to achieve strong EM protection.

PIN diode is controlled by the average power of the incident wave and does not require a bias circuit for an adaptive response. When the low-power working signal passes through, the diode is in the cut-off state, which is equivalent to a small capacitor. When affected by an interference signal with a power exceeding the threshold, the diode conducts and exhibits a small resistance in series. By incorporating a diode into the slotline structure, the diode operates in different states when EM waves with different powers are incident.

The loading of an inductor at the center of the slotline is primarily to create multiple resonant points. Owing to the structural symmetry, this study introduces an even-odd mode analysis method to simplify the two-port network into two types of single-port networks. The specific structure is shown in Figs. 1(a)–(c).

Specifically, when the structure is in a transparent state and the diode is not conducting, it is equivalent to a junction capacitance C_{PIN}. The equivalent circuit can be decomposed into distinct responses: odd-mode and even-mode excitations, as shown in Fig. 2.

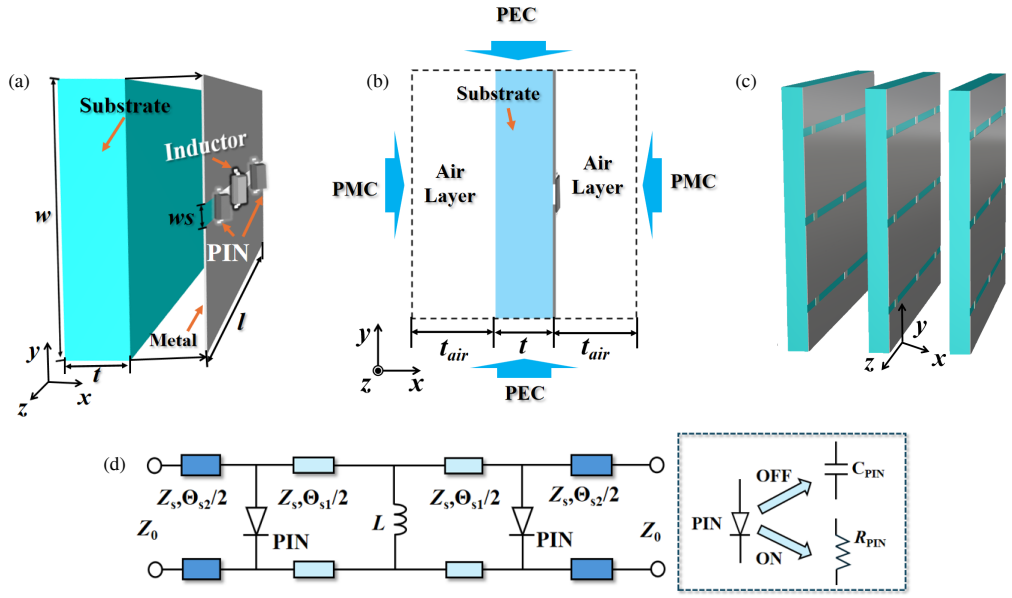

FIGURE 1. Geometry of the proposed ESS with two resonant points. (a) Perspective 3-D view, (b) side view of a unit cell and boundary condition settings, (c) periodic array, and (d) equivalent circuit of the proposed ESS.

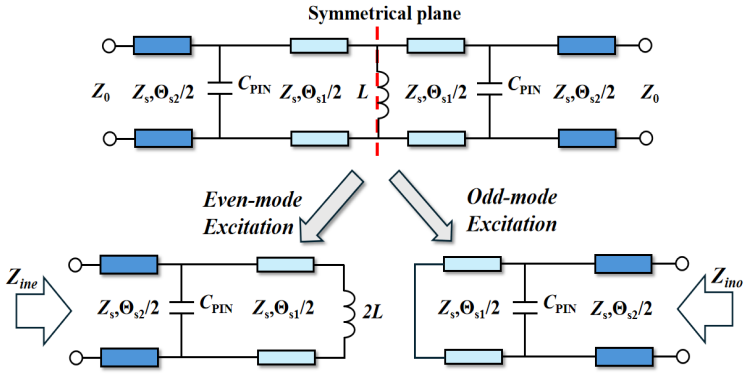

FIGURE 2. Equivalent TL model of the ESS in transparent state.

Following the equivalent circuit framework introduced in [23], the input even and odd mode impedances are

$$Z_{ine} = jZ_s \frac{\tan\Theta_{s2} + Z_1\left(1 - Z_s B_c \tan\Theta_{s2}\right)}{1 - Z_1\left(Z_s B_c + \tan\Theta_{s2}\right)}, \quad (1)$$

$$Z_{ino} = jZ_s \frac{\tan\frac{\Theta_{s1}}{2} + \tan\Theta_{s2} - B_c Z_s \tan\frac{\Theta_{s1}}{2}\tan\Theta_{s2}}{1 - \tan\frac{\Theta_{s1}}{2}\tan\Theta_{s2} - B_c Z_s \tan\frac{\Theta_{s1}}{2}}, \quad (2)$$

where

$$Z_1 = \left(X_{2L} + Z_s \tan\frac{\Theta_{s1}}{2}\right) / \left(Z_s - X_{2L}\tan\frac{\Theta_{s1}}{2}\right), \quad (3)$$

$$B_c = (2\pi f) C_{PIN}, \quad (4)$$

Based on Eqs. (1)–(2), the scattering parameters can also be obtained as follows,

$$S_{11} = \frac{Z_{ine}Z_{ino} - Z_0^2}{\left(Z_{ine} + Z_0\right)\left(Z_{ino} + Z_0\right)}, \quad (5)$$

$$S_{21} = \frac{Z_0\left(Z_{ine} - Z_{ino}\right)}{\left(Z_{ine} + Z_0\right)\left(Z_{ino} + Z_0\right)}, \quad (6)$$

By substituting $S_{11} = 0$, that is $Z_{ine}Z_{ino} = Z_0^2$, the analytical values of the two resonant points in the passband can be calculated using MATLAB.

As shown in Fig. 3, the current at f_1 flows through the loaded inductor, whereas the surface current at f_2 flows from one end of the slotline to the other end. According to the discussion in [25], it can be concluded that f_1 is mainly due to the resonance of half of the slotline, diodes, and inductors, which is caused by an even-mode resonator as shown in Fig. 3(a). f_2 is mainly determined by the resonance of the entire slotline and diode, which is caused by the odd-mode resonator, as shown in Fig. 3(b).

The even-mode resonance point is determined by the port impedance, characteristic impedance of the slotline Z_s, inductance value L, relative position of the diodes l_s, length of the slotline $l_{slotline}$, and junction capacitance of the diodes C_{PIN}. The odd-mode resonance point depends on the same factors as

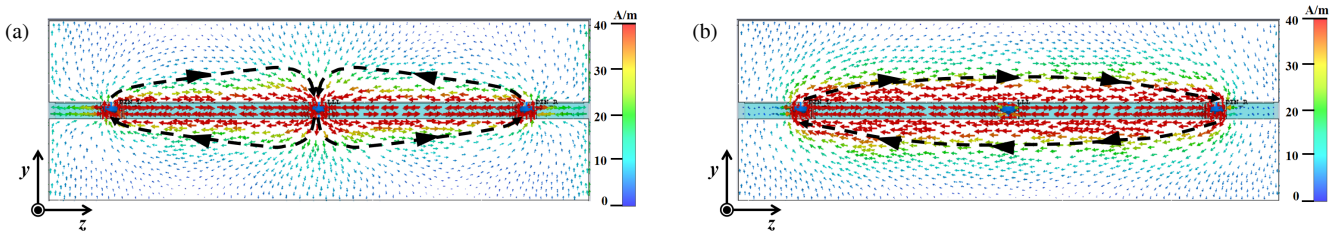

FIGURE 3. Schematic diagram of current distribution on the xoy plane at resonance frequency f_1 and f_2.

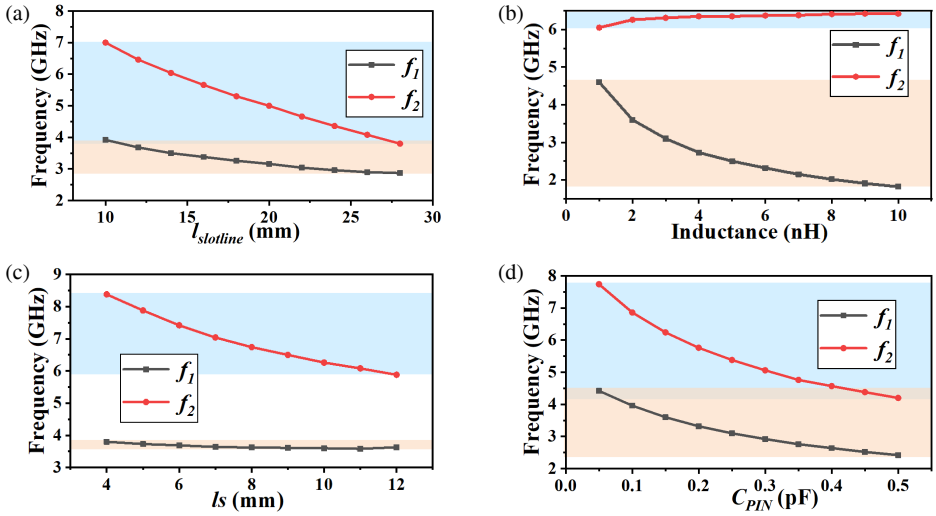

FIGURE 4. Several key influencing parameters on transmission characteristics. (a) The length of the slotline $l_{slotline}$, (b) inductance value of inductor L, (c) distance between diodes l_s, and (d) equivalent junction capacitance of diode C_{PIN}.

the even-mode, except for the inductance value. In addition, the relationship between port impedance Z_0 and characteristic impedance of slotline Z_s can affect the flatness of the transmission passband. Z_0 mainly depends on the air layer spacing t_{air} and the width of the structural unit w. Z_s is the transmission impedance of the slotline, and its key influencing factors are slotline width w_s and dielectric constant $\mathcal{E}_r$ of the substrate. To prove the above conclusion, the influence curves of several key influencing parameters on the transmission characteristics are shown in Fig. 4.

As shown in Fig. 4(a), when the type of PIN diode is determined, as the length of the slotline $l_{slotline}$ increases, the two resonant frequencies decrease. Both odd- and even-mode resonant circuits are related to the overall length of the slotline. The range of the entire passband can be manipulated by adjusting the length of the slotline.

In Figs. 4(b)–(c), when other parameters are kept constant, the resonant point f_1 is more sensitive to the change in the inductance value of the inductor, whereas the resonant point f_2 is more sensitive to the relative distance loaded between the diodes. That is, the two resonant frequencies can be controlled by independently adjusting the inductance value L of the loaded inductor and relative distance l_s.

The influence of the loaded diodes on the passband mainly depends on the equivalent junction capacitance C_{PIN} of the diode. As shown in Fig. 4(d), the resonant frequency of the structure decreases as the capacitance C_{PIN} increases, thereby adjusting the operating frequency band of the overall selectable structure.

As shown in Figs. 5(a)–(d), the parameters w and air spacing t_{air} affect the input impedance Z_0, whereas the dielectric constant $\mathcal{E}_r$ and slotline width w_s affect Z_s, thereby jointly affecting the impedance matching effect. The larger the dielectric constant, the greater the parasitic capacitance of the slotline transmission line, which lowers the resonant frequency of the structure. This, in turn, affects the flatness between the resonance points of the transmission curve, which has an impact on the design of the transmission passband bandwidth of subsequent high-performance ESS. It can also be observed in the figure that the higher-frequency resonance point has a more significant impact on the width of the groove line than the lower-frequency resonance point and can be used as a key optimization variable. However, considering the width requirements for assembling diodes, w_s must be fixed in the structural design.

When the structure is subjected to the input of a strong EM wave, the strong EM energy induces a voltage across the two diode terminals. When the induced voltage exceeds the conduction threshold of the diode, the diode enters a conductive state. Consequently, a transition from a high-impedance to a low-impedance state is achieved. At this time, the diode can be equivalent to a resistor, and its equivalent circuit is shown in Fig. 6.

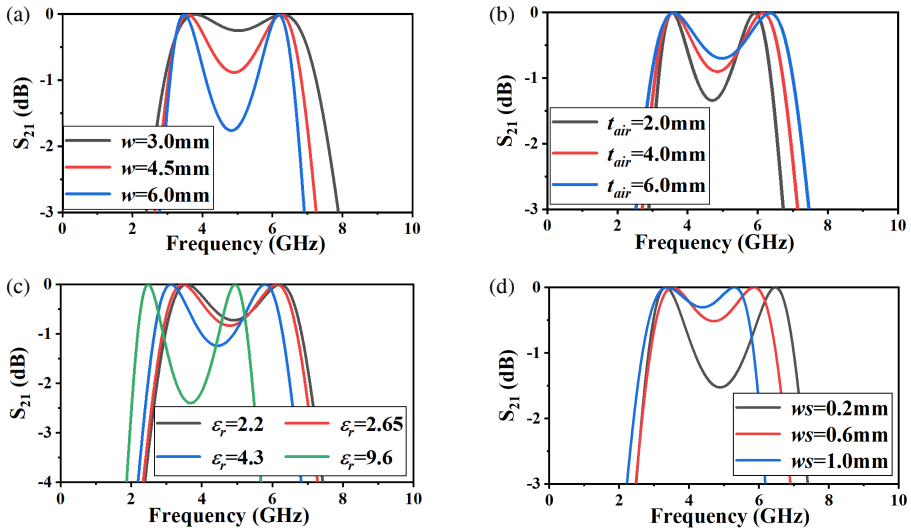

FIGURE 5. The impact of key parameters on the transmission passband. (a) Periodic unit width w, (b) the thickness of the air layer t_{air}, (c) the dielectric constant of substrate $\mathcal{E}_r$, and (d) slotline width w_s.

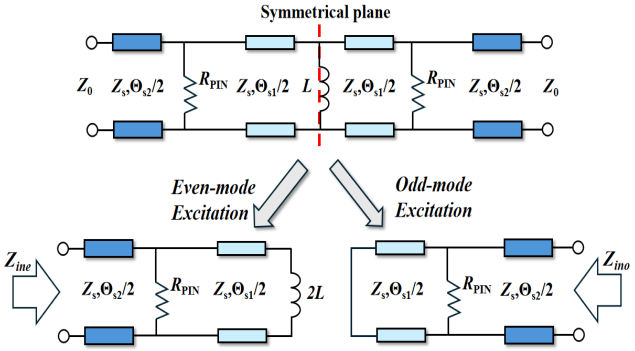

FIGURE 6. Equivalent TL model of the ESS in shielding state.

Based on the above analysis, the even and odd mode impedance of this symmetric structure is

$$Z_{ine}=jZ_s\cdot\frac{jZ_1Z_s\tan\Theta_{s2}+R\left(Z_1+\tan\Theta_{s2}\right)}{jZ_1Z_s+R\left(1-Z_1\tan\Theta_{s2}\right)}, \tag{7}$$

$$Z_{ino}=jZ_s\cdot\frac{jZ_s\tan(\Theta_{s1}/2)\tan\Theta_{s2}+R\left(\tan\left(\Theta_{s1}/2\right)+\tan\Theta_{s_2}\right)}{jZ_s\tan\left(\Theta_{s1}/2\right)+R\left(1-\tan\left(\Theta_{s1}/2\right)\right)\tan\Theta_{s_2}}, \tag{8}$$

where

$$Z_1=\tan\left(\Theta_{s1}/2\right), \tag{9}$$

By substituting the results into Equations (5)–(6), numerical solutions can be obtained using MATLAB. Owing to the complexity of the structure, accurate analytical expressions cannot be obtained. Through simulation, the effects of the following three key parameters on the transmission curve were obtained, as shown in Fig. 7. From the perspective of circuit principles, the resistor is connected in parallel to the TL structure. During the signal-transmission process, the smaller the resistance value, the more obvious the current-sharing effect. According to the current-sharing principle of a parallel circuit, more current flows through the resistance, resulting in a significant reduction in the current flowing to the subsequent circuit. From the perspective of the transmission coefficient, the signal power reaching the output port was significantly reduced. Therefore, the value dropped sharply, indicating that the transmission ability deteriorated.

As shown in Fig. 7(a), when the diode was turned on, the overall structure exhibited a protective state, and a decrease in the equivalent resistance R of the diode significantly increases the SE. Fig. 7(b) shows that reducing air gap t_{air} also enhances the SE. As illustrated in Fig. 7(c), increasing the distance l_s between the diodes changes the relationship between the spacing and the wavelength, which significantly alters the frequency response of the circuit. Specifically, as l_s increases, the transmission coefficient decreases, resulting in higher SE.

To characterize the nonlinear response process of the structure, Fig. 8 shows S_{21} curves of the unit structure at different frequencies and input powers. As the power of S_{21} continues to increase, the transmittance of the entire structure decreases, thereby achieving greater shielding effectiveness, indicating the adaptive protection characteristics of the ESS.

3. DESIGN OF HIGH-PERFORMANCE ENERGY-SELECTIVE STRUCTURE

3.1. Design Guidelines

Summarizing the above simulation analysis, the following conclusions can be drawn:

1. The central operating frequency of the overall structure can be adjusted by modifying the slotline length $l_{slotline}$.

2. The dual-resonance frequencies can be independently adjusted by changing the inductance value of the inductor L and diode spacing l_s. Simultaneously, the parameter l_s can also adjust the size of the SE.

3. The air gap, t_{air}, and unit width, w, can be used to adjust the impedance variation, thereby regulating the passband flatness of the structure.

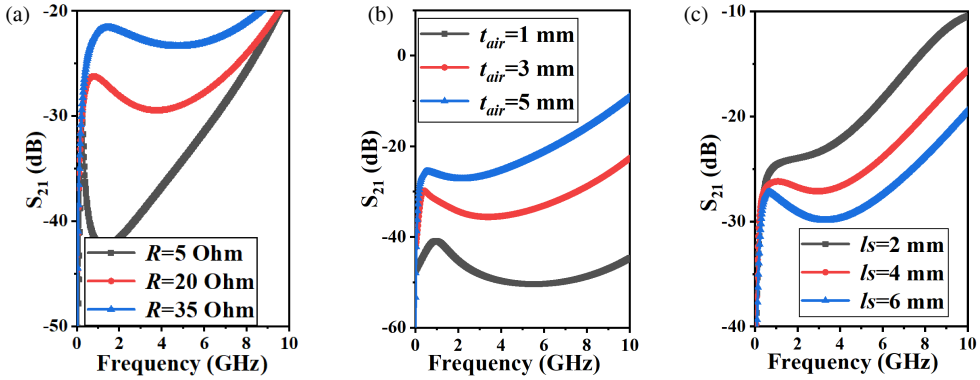

FIGURE 7. The impact of key parameters on the transmission passband. (a) Equivalent resistance of diode R_{PIN}, (b) the thickness of the air layer t_{air}, and (c) the distance between diodes l_s.

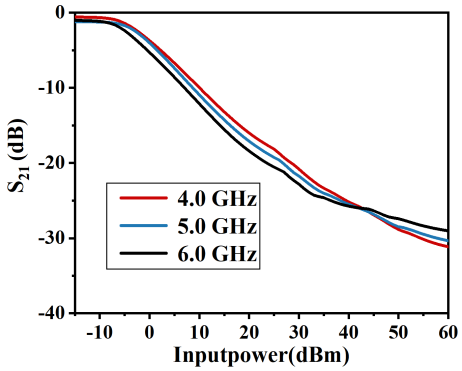

FIGURE 8. S_{21} curves of unit structures at different frequencies and input powers.

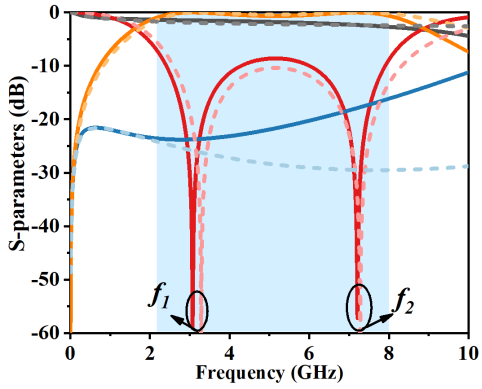

FIGURE 9. S-parameter results from CST-MWS and equivalent TL model for the ESS unit (physical dimensions: $l = 13\,\text{mm}$, $ws = 0.4\,\text{mm}$, $w = 3.0\,\text{mm}$, $l_s = 8\,\text{mm}$, $t = 1\,\text{mm}$, $t_{air} = 4.5\,\text{mm}$, and $\mathcal{E}_r = 2.65$; corresponding electrical parameters: $L = 3.3\,\text{nH}$, $C_{PIN} = 0.15\,\text{pF}$, $R_{PIN} = 14\,\Omega$, $Z_s = 73.4\,\Omega$, $Z_0 = 112.6\,\Omega$, $\Theta_s = 180°$ at 10.0 GHz). Solid lines represent CST full-wave simulation results, while dashed lines correspond to ADS equivalent circuit model results. Red lines indicate S_{11} in the OFF state, gray lines indicate S_{11} in the ON state, orange lines indicate S_{21} in the OFF state, and blue lines indicate S_{21} in the ON state.

TABLE 1. Parameters correlation relationship.

Parameters	f_1	f_2	IL	SE
Inductance of the inductor L	↓	/	/	/
Unit length $l_{slotline}$	↓	↓	/	/
Unit width w	/	/	↑	/
The spacing between diodes l_s	/	↓	/	↑
Air layer spacing t_{air}	/	/	↓	↓
Junction capacitance of the diode C_{PIN}	↓	↓	/	/
Conduction resistance of the diode R_{PIN}	/	/	/	↓

4. A smaller air gap t_{air} between the units leads to a higher SE. However, it also deteriorates the curve flatness between the resonance points, which affects the passband width. Therefore, the air gap, t_{air}, must be optimized through a trade-off based on the design requirements.

5. From the perspective of diode selection, the lower the junction capacitance C_{PIN}, the smaller the impact on the passband and the wider the frequency band that can be achieved. According to the requirements of energy-based structural protection, the SE within the passband must be maximized. The smaller the equivalent resistance R_{PIN} of the diode, the higher the SE.

The correlation relationships of the parameters are shown in Table 1. The coupling degree between the inductance value of the inductor and the distance between the diodes was relatively low. These two parameters can achieve decoupling of the control of resonant frequency points. Thus, further combining with the requirements of application scenarios, flexibly adjusting the distribution of resonance points.

3.2. Design of Ultra-Wideband Energy-Selective Structure (UWB ESS)

To optimize the bandwidth performance, the inductance of the loaded inductor should be increased to shift the resonance frequency to a lower range. Meanwhile, the diode spacing should be minimized to increase the position of the resonance frequency, causing the resonance frequencies to gradually separate. To ensure that the insertion loss (IL) is within 1 dB, the concession of the passband between the frequencies should be reduced as much as possible; therefore, increasing the spacing between the cells, t_{air}, is an effective method.

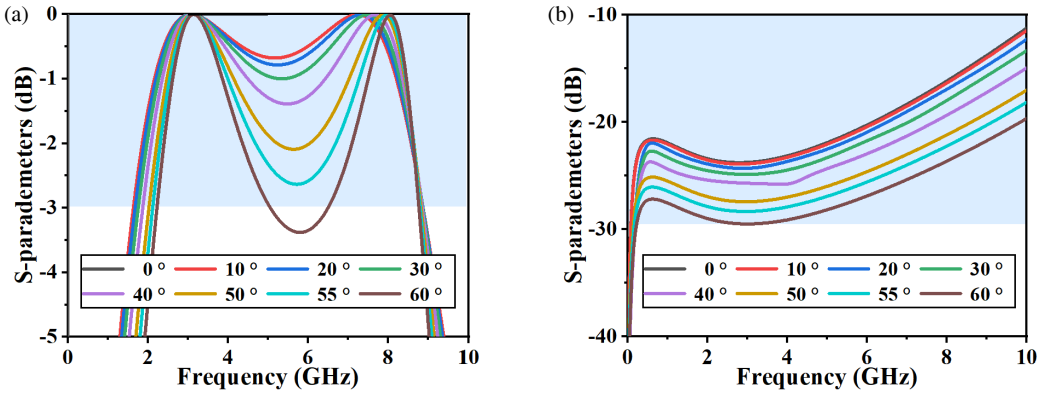

FIGURE 10. S_{21} curves under different angles of UWB ESS. (a) Transparent state and (b) Shielding state.

Because the SE and passband flatness are mutually restrictive with respect to the parameter, the passband flatness between the frequencies should be improved as much as possible while ensuring that the shielding effectiveness is above the minimum of 10 dB.

The NSR201 diode, with a junction capacitance of 0.15 pF and equivalent resistance of 14 Ω, was adopted in this design. The unit-structure parameters and transmission characteristics after design and optimization in Fig. 9 show that the structure can achieve an IL of less than 1 dB in the 2.2–8.0 GHz range. Moreover, it has a protection capability of over 15.6 dB across the entire bandwidth, with a relative bandwidth of 113.7%. The OFF state in the figures represents the transparent state, and the ON state represents the shielded state.

Because the structural design is aimed at a single TE polarization form, the angle stability of the article is discussed in the form of TE polarization. In order to further investigate the angular stability of the UWB ESS, simulations were conducted for S_{21} with different angles in TE polarization, and the simulation results are shown in Fig. 10. Although the angle stability under ultra-wideband is difficult to maintain, the structure can still maintain 3 dB angle stability within 55° under transparent conditions, and its protective ability can also be improved. Under oblique incidence, the UWB ESS's performance degrades due to several factors. A longer equivalent propagation path pulls the resonance downward, while the changing free-space wave impedance causes impedance mismatch and raises IL. Grating lobes become an issue at large angles, either limiting the usable high-frequency bandwidth or leaking energy. The effective spacing between stacked layers also changes, which weakens interlayer coupling and harms passband flatness.

3.3. Design of Energy-Selective Structure with High Shielding Efficiency (HSE ESS)

To achieve the design goal of maximizing the SE, the air gap, t_{air}, must be minimized as much as possible. However, this also implies that the dip in the passband curve between the frequency points will worsen. Therefore, it is necessary to reduce the interval between the two frequency points, sacrificing a certain bandwidth to achieve a larger SE. The diode should have a low turn-on threshold and a high power tolerance. The NSR201 diode was selected for loading.

The equivalent circuit simulation results in Advanced Design System (ADS) simulation software are consistent with the full-wave simulation results in Computer Simulation Technology (CST). As shown in Fig. 11, the results indicate that the proposed ESS structure in simulation can achieve IL below 1 dB in the range of 3.9–6.2 GHz (relative bandwidth of 45.5%), while also providing over 40 dB of shielding capability.

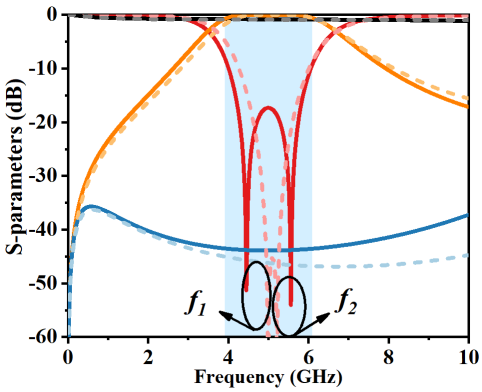

FIGURE 11. S-parameter results from CST-MWS and equivalent TL model for the ESS unit (S-parameter results from CST-MWS and equivalent TL model for the ESS unit (Different parameters from UWB structure: $l_s = 10$ mm, $t_{air} = 1.5$ mm, $L = 1.2$ nH, $Z_s = 121.7\,\Omega$, $Z_0 = 280.1\,\Omega$). Solid lines represent CST full-wave simulation results, while dashed lines correspond to ADS equivalent circuit model results. Red lines indicate S_{11} in the OFF state, gray lines indicate S_{11} in the ON state, orange lines indicate S_{21} in the OFF state, and blue lines indicate S_{21} in the ON state.

Figure 12 shows the S_{21} curves under different angles in two different states. Due to its narrower bandwidth compared to UWB ESS, HSE ESS can maintain better 3 dB angle stability below 65° in a transparent state, and its protection capability improves with an increasing angle.

4. FABRICATION AND MEASUREMENT

In order to measure the EM response of the structure to signals of different intensities, the IL of the ESS structure was tested by employing the spatial field windowing method, and the strong-field response of the structure was tested using the waveguide

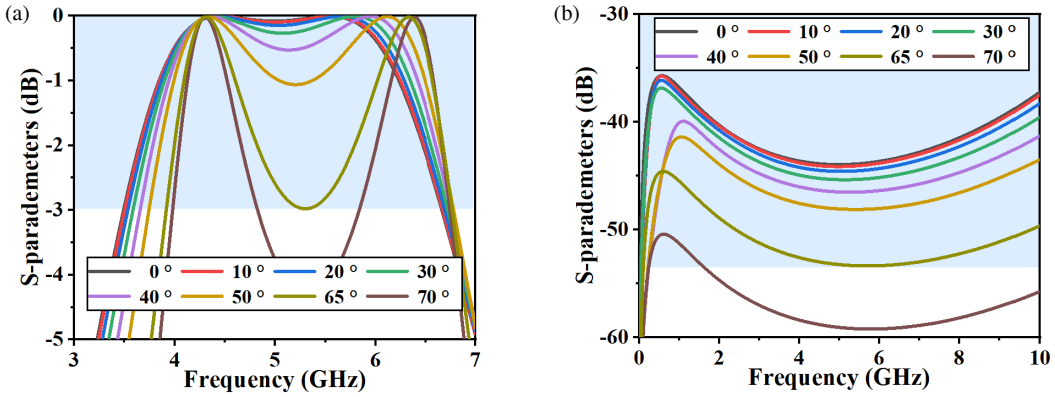

FIGURE 12. S_{21} curves under different angles of HSE ESS. (a) Transparent state; (b) Shielding state.

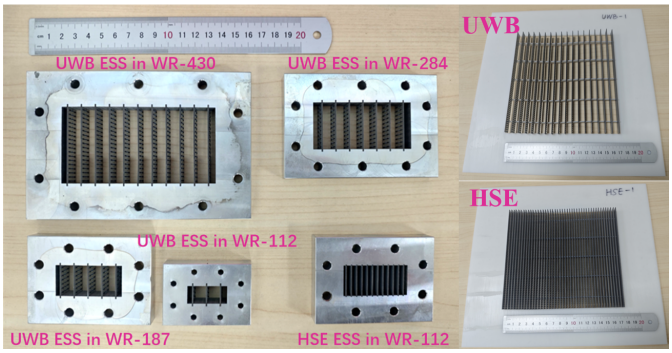

FIGURE 13. Schematic diagram of placement of waveguide inserts.

injection method. The experimental setup was connected as shown in Fig. 13.

High-performance ESS can be fabricated using PCB technology, where a metal frame structure with etched grooves is employed to maintain precise spacing between units. By appropriately adjusting the dimensions of the unit structure to match the size of the waveguide DUT port, the components were integrated to form the internal test plug-in structure of the waveguide. It is important to note that verifying the SE across the UWB ESS broadband requires testing with several waveguides. The following content will be tested and verified in two ways: low power and high power.

4.1. Low-Power Signals Measurements

First, standard horn antennas were connected to the two ports of the vector network analyzer and calibrated with low-power signals using the windowing method. Then, the transmission response of the ESS is measured after extending the window loading period and is denoted as IL.

The simulated and measured results of the IL are shown in Fig. 15. It can be seen that the trend is consistent across the entire frequency band. Under the experimental conditions, Prototype I, designed for ultra-wideband, achieved an IL below 1 dB in the frequency band range of 2.2–8.2 GHz, with a relative bandwidth of 115.4%. Prototype II, designed for a high SE, achieved an IL below 1 dB in the frequency band range of 3.9–6.3 GHz, with a relative bandwidth of 47.1%.

The experimental and simulated results for the designed working band were consistent. The measured bandwidth of the structure was slightly wider than the simulation results because the spacing between the diodes significantly affected the bandwidth, and insufficient manufacturing accuracy led to this situation. In summary, both structures under one model can achieve a broadband design.

4.2. High-Power Signals Measurements

As shown in Fig. 14, the pulse signal generated by the signal source (with a pulse width ratio of 1%) was amplified by a power amplifier to increase the EM wave power entering the waveguide. By connecting a three-port ringer and matching the load, the energy reflected into the amplifier was reduced to prevent damage. Subsequently, the waveguide, attenuator (to reduce the power of the EM waves entering the spectrograph), and spectrograph were connected through RF cables. By recording readings of the spectrograph during the no-load operation, the SE can be obtained by comparing readings of the loaded ESS plug-ins.

The two types of ESSs at various frequency points are measured within the bandwidth, and the simulated and experimental results were compared, as shown in Fig. 15. The SE of Prototype I within the entire bandwidth was higher than 10 dB. The SE of Prototype II is higher than 33 dB across the entire bandwidth, and the maximum SE can reach 40.3 dB.

To further illustrate the nonlinear response characteristics of the ESSs, Fig. 16 shows the curve of the SE as a function of the power injected into the waveguide. As the input power increased for each frequency point, the entire SE showed an increasing trend; the diode was not fully conducting; and the ESSs did not reach saturation. Owing to the limited power output of the power amplifier, the measured SE was not as high as the simulated SE. Since the high-power measurements were conducted inside a waveguide, the transverse electric field distribution is nonuniform, with a stronger field at the center and a weaker field near the edges. Therefore, at the maximum input power, only the diodes near the center reached stable conduction, while the edge diodes remained partially conducting due to the weaker local electric field. This nonuniform field distribution explains the relatively stable SE observed at certain input

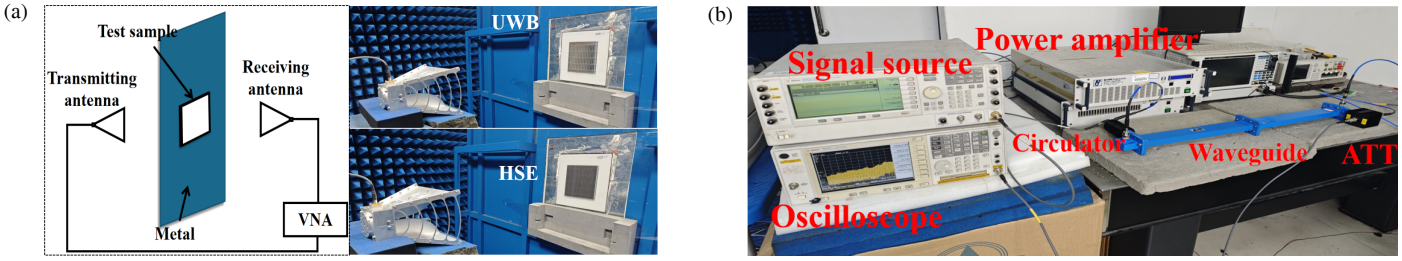

FIGURE 14. Testing setup and the ESS prototypes. (a) IL testing setup in waveguides and (b) SE testing setup in waveguides.

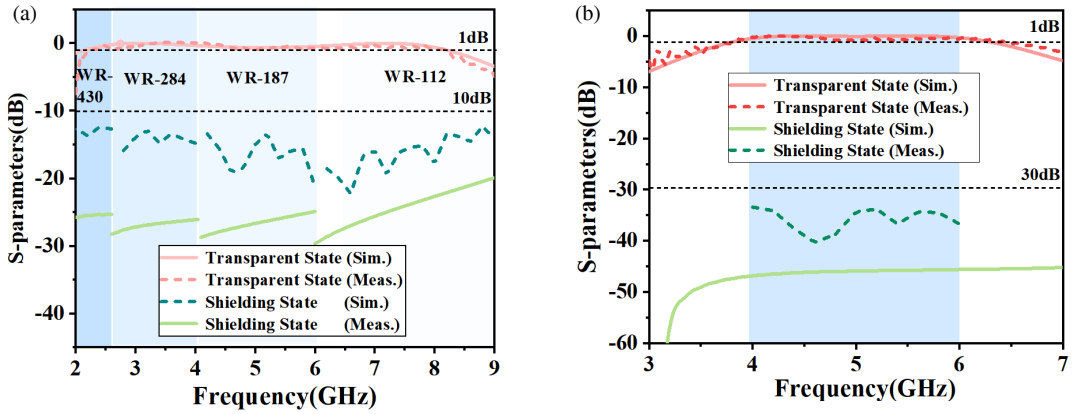

FIGURE 15. The results of the ESS structure. (a) UWB sample; (b) HSE sample.

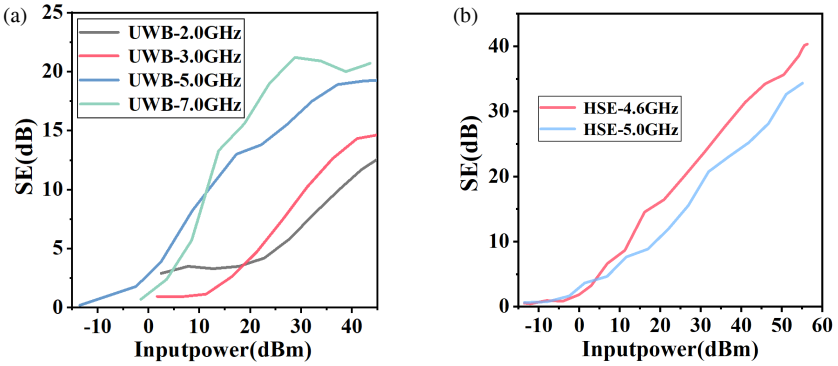

FIGURE 16. SE curves with input power variation at different frequency points. (a) UWB sample and (b) HSE sample.

power levels. At higher frequencies, the stronger local electric field enables the diodes to enter the conducting state more easily. As the input power further increases, the SE is expected to improve continuously as more diodes gradually become fully conductive.

4.3. Comparison

A comparison between our proposed ESS and those in other studies is listed in Table 2. In this table, passband bandwidth is the frequency range where ESS allows signals to pass under low-power conditions with low insertion loss (IL $<$ 1 dB) to ensure normal operation, while shielding bandwidth is the range where ESS effectively blocks high-power signals with shielding effectiveness (SE) above a threshold (e.g., $>$ 10 dB); the ESS performance is defined by the intersection where IL $<$ 1 dB and SE $>$ 10 dB, recognized as the working frequency band.

In this study, two types of high-performance ESSs were designed based on the same topological structure. Prototype I is designed for ultra-wideband applications and achieves a working band range of over 100%. Prototype II is developed to achieve high SE and reaches an SE above 40 dB within the wideband range. Although Prototype I covers a wide frequency range, its angular stability (3 dB) can still reach a relatively high level. Narrowband Prototype II can achieve angle stability within 65°, fully demonstrating the high angle stability performance of this slotline-type structure. The targeted indicators of these two high-performance ESSs are far superior to those of other similar designs, which fully demonstrates the effectiveness and great application potential of the design method proposed in this study.

TABLE 2. Comparison of the proposed ESS with others in the literature.

Ref.	IL (dB)	SE (dB)	Passband bandwidth	Shielding bandwidth	Unit cell (λ_0^3)	Angular stability
[10]	< 1	> 18	< 1.1 GHz	< 1.5 GHz	$0.01 \times 0.01 \times 0.003$ (1 GHz)	—
[12]	< 1	> 10	6.7–10.8 GHz (46.9%)	6.7–10.8 GHz	$0.46 \times 0.03 \times 0.44$	—
[22]	0.6	> 40	3 GHz	2.0–4.0 GHz	$0.30 \times 0.16 \times 0.13$	0°–30° (2 dB)
[23]	< 1	> 30, Max=32	4.1–5.3 GHz (25.5%)	0–5.3 GHz (200%)	$0.08 \times 0.08 \times 0.28$	0°–45° (1 dB)
[26]	< 1	> 23	6.0–10.0 GHz (50%)	0–16 GHz (200%)	$0.20 \times 0.20 \times 0.15$	0°–40° (3 dB)
[27]	< 1	> 20	5.2–14.5 GHz (91.1%)	0–15^+ GHz (200%)	$0.17 \times 0.17 \times 0.13$	0°–40° (1 dB)
[28]	< 1	> 20	6.3–12.2 GHz (63.8%)	0–12.2^+ GHz (200%)	$0.20 \times 0.12 \times 0.095$	0°–60° (3 dB)
[29]	< 1	> 22	5.8–9.0 GHz (43.2%)	0–12^+ GHz (200%)	$0.09 \times 0.09 \times 0.07$	0°–55° (3 dB)
Pro. I	< 1	> 10	**2.2–8.2 GHz (115.4%) Meas.**	0–8.2 GHz (200%) Meas.	$0.17 \times 0.05 \times 0.22$	0°–30° (1 dB), 0°–55° (3 dB)
Pro. II	< 1	**>33, Max = 40.3**	**3.9–6.3 GHz (47.1%) Meas.**	0–6.3 GHz (200%) Meas.	$0.06 \times 0.05 \times 0.22$	0°–50° (1 dB), 0°–65° (3 dB)

5. CONCLUSION

This paper has presented a design methodology for high-performance ESS based on slotline structures. In this approach, an accurate equivalent circuit model was built, and the key factors affecting ESS performance were identified, which together form systematic design guidelines. Based on these guidelines, two prototype structures were designed and experimentally tested, confirming that the method can achieve an ultra-wideband working band and high SE. However, the performance relied on the precise control of circuit and semiconductor parameters, as well as fabrication accuracy, which may limit its use at extremely low or high frequencies. To address these limitations, future work will focus on combining wide operating bandwidth with high SE, exploring tunable or adaptive ESS designs, and extending the methodology to more complex structures for broader practical applications.

REFERENCES

[1] Tyo, J. S., "High power electromagnetic radiators: Nonlethal weapons anod other applications [Reviews and Abstracts]," *IEEE Antennas and Propagation Magazine*, Vol. 48, No. 6, 130–131, 2006.

[2] Chang, C., G. Liu, C. Tang, C. Chen, and J. Fang, "Review of recent theories and experiments for improving high-power microwave window breakdown thresholds," *Physics of Plasmas*, Vol. 18, No. 5, 055702, 2011.

[3] Elluru, D. N., A. K. Awasthi, S. P. Gogineni, D. Taylor, A. Shahabi, A. N. Lemmon, C. Chung, and J. Lee, "Design of an absorptive high-power PIN diode switch for an ultra-wideband radar," *IEEE Journal of Microwaves*, Vol. 2, No. 2, 286–296, 2022.

[4] Yang, L., L.-A. Yang, T. Rong, Y. Li, Z. Jin, and Y. Hao, "Codesign of K a-band integrated GaAs PIN diodes limiter and low noise amplifier," *IEEE Access*, Vol. 7, 88 275–88 281, 2019.

[5] Tseng, C.-C. and S.-L. Lee, "Minimax design of graph filter using Chebyshev polynomial approximation," *IEEE Transactions on Circuits and Systems II: Express Briefs*, Vol. 68, No. 5, 1630–1634, 2021.

[6] Zechmeister, J. and J. Lacik, "Automatic design procedure of waveguide filters based on a pixelization strategy," *IEEE Microwave and Wireless Technology Letters*, Vol. 33, No. 10, 1423–1425, 2023.

[7] Hakim, M. L., M. T. Islam, and T. Alam, "Incident angle stable broadband conformal mm-wave FSS for 5G (n257, n258, n260, and n261) band EMI shielding application," *IEEE Antennas and Wireless Propagation Letters*, Vol. 23, No. 2, 488–492, 2024.

[8] Li, Y., P. Ren, Z. Xiang, B. Xu, and R. Chen, "Design of dual-stopband FSS with tightly spaced frequency response characteristics," *IEEE Microwave and Wireless Components Letters*, Vol. 32, No. 8, 1011–1014, 2022.

[9] Sen, G., M. Midya, and S. Ghosh, "Design of a band pass FSS with a sharp transition response based on SIW technology for satellite application," in *2021 5th International Conference on Electronics, Materials Engineering & Nano-Technology (IEMENTech)*, 1–3, Kolkata, India, 2021.

[10] Yang, C., P.-G. Liu, and X.-J. Huang, "A novel method of energy selective surface for adaptive HPM/EMP protection," *IEEE Antennas and Wireless Propagation Letters*, Vol. 12, 112–115, 2013.

[11] Wen, K., X. Huang, T. Tian, W. Huang, and P. Liu, "Design and demonstration of high-power density infrared nonlinear filtering window with EM shielding," *Optics Express*, Vol. 32, No. 4, 5956–5968, 2024.

[12] Huang, R., J. Liu, C. Liu, Y. Xu, and S. Zha, "A broadband adaptive waveguide high-power microwave protector," *IEEE Mi-*

crowave and Wireless Technology Letters, Vol. 33, No. 1, 15–18, 2023.

[13] Jiang, H., B. Deng, Y. Xu, T. Tian, and P. Liu, "Ultrawideband energy-selective structure based on spoof surface plasmon polariton," *IEEE Antennas and Wireless Propagation Letters*, Vol. 24, No. 3, 537–541, 2025.

[14] Luo, G. Q., W. Hong, Q. H. Lai, K. Wu, and L. L. Sun, "Design and experimental verification of compact frequency-selective surface with quasi-elliptic bandpass response," *IEEE Transactions on Microwave Theory and Techniques*, Vol. 55, No. 12, 2481–2487, 2007.

[15] Wang, D. S., B. J. Chen, and C. H. Chan, "High-selectivity bandpass frequency-selective surface in terahertz band," *IEEE Transactions on Terahertz Science and Technology*, Vol. 6, No. 2, 284–291, 2016.

[16] Yan, M., J. Wang, H. Ma, M. Feng, Y. Pang, S. Qu, J. Zhang, and L. Zheng, "A tri-band, highly selective, bandpass FSS using cascaded multilayer loop arrays," *IEEE Transactions on Antennas and Propagation*, Vol. 64, No. 5, 2046–2049, 2016.

[17] Ferreira, D., R. F. S. Caldeirinha, I. Cuiñas, and T. R. Fernandes, "Square loop and slot frequency selective surfaces study for equivalent circuit model optimization," *IEEE Transactions on Antennas and Propagation*, Vol. 63, No. 9, 3947–3955, 2015.

[18] Chen, G.-W., S.-W. Wong, Y. Li, R.-S. Chen, L. Zhang, A. K. Rashid, N. Xie, and L. Zhu, "High roll-off frequency selective surface with quasi-elliptic bandpass response," *IEEE Transactions on Antennas and Propagation*, Vol. 69, No. 9, 5740–5749, 2021.

[19] Rashid, A. K. and Z. Shen, "A novel band-reject frequency selective surface with pseudo-elliptic response," *IEEE Transactions on Antennas and Propagation*, Vol. 58, No. 4, 1220–1226, 2010.

[20] Shen, Z., J. Wang, and B. Li, "3-D frequency selective rasorber: Concept, analysis, and design," *IEEE Transactions on Microwave Theory and Techniques*, Vol. 64, No. 10, 3087–3096, 2016.

[21] Omar, A. A. and Z. Shen, "Double-sided parallel-strip line resonator for dual-polarized 3-D frequency-selective structure and absorber," *IEEE Transactions on Microwave Theory and Techniques*, Vol. 65, No. 10, 3744–3752, 2017.

[22] Zhou, L. and Z. Shen, "3-D absorptive energy-selective structures," *IEEE Transactions on Antennas and Propagation*, Vol. 69, No. 9, 5664–5672, 2021.

[23] Jiang, H., B. Deng, S. Zha, T. Tian, and P. Liu, "Energy selective structure with high shielding efficiency based on slotline," *IEEE Microwave and Wireless Technology Letters*, Vol. 35, No. 8, 1182–1185, 2025.

[24] Li, B. and Z. Shen, "Three-dimensional bandpass frequency-selective structures with multiple transmission zeros," *IEEE Transactions on Microwave Theory and Techniques*, Vol. 61, No. 10, 3578–3589, 2013.

[25] Hong, J. and M. J. Lancaster, *Microstrip Filters for RF/Microwave Applications*, John Wiley & Sons, 2001.

[26] Tian, T., X. Huang, Y. Xu, P. Liu, C. Liu, N. Hu, J. Zhang, and Z. Wu, "A wideband energy selective surface with quasi-elliptic bandpass response and high-power microwave shielding," *IEEE Transactions on Electromagnetic Compatibility*, Vol. 66, No. 1, 224–233, 2024.

[27] Wu, Z., Y. Xu, P. Liu, T. Tian, and M. Lin, "An ultra-broadband energy selective surface design method: From filter circuits to metamaterials," *IEEE Transactions on Antennas and Propagation*, Vol. 71, No. 7, 5865–5873, 2023.

[28] Zhang, J., F. Kang, Z. Liu, Z. Qu, M. Xu, S. Zha, and P. Liu, "Design of ultrawideband energy selective surface based on triple-layer structure and semiconductor for HIRF prevention," *IEEE Transactions on Antennas and Propagation*, Vol. 73, No. 11, 9619–9624, 2025.

[29] Zhou, T., P. Liu, C. Liu, H. Jiang, and T. Tian, "Multilayer energy selective surface with wide operational band and high shielding effectiveness based on second-order filter," *IEEE Transactions on Electromagnetic Compatibility*, Vol. 67, No. 1, 337–340, 2025.

[30] Wu, Z., P. Liu, M. Lin, S. Zha, and X. Ni, "A microwave field-induced nonlinear metamaterial with wafer integration level," *ACS Applied Materials & Interfaces*, Vol. 15, No. 12, 16 189–16 197, 2023.